Nano Research

Open Access

Research Article

Bias-controlled vertical asymmetrical dual-Schottky junction photodetectors for direct linear polarimetry and AoLP imaging

Lingxian Kong[1], Qi Su[2], Shijie Wang[2], Zhiyong Liu[1], Guanglan Liao[1], Bo Sun[2,3] ✉, and Tielin Shi[1] ✉

[1] *State Key Laboratory of Digital Manufacturing Equipment and Technology, Huazhong University of Science and Technology, Wuhan 430074, China*
[2] *School of Aerospace Engineering, Huazhong University of Science and Technology, Wuhan 430074, China*
[3] *Shenzhen Huazhong University of Science and Technology Research Institute, Shenzhen 518057, China*

Cite this article: *Nano Research*, **2025**, *18*, 94907392. https://doi.org/10.26599/NR.2025.94907392

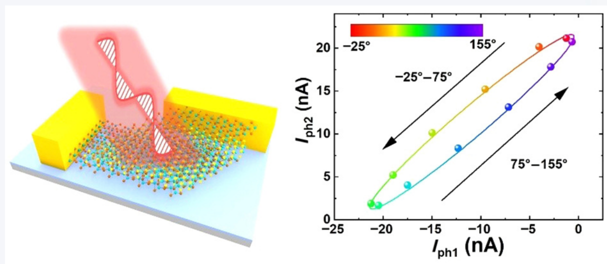

ABSTRACT: Anisotropic two-dimensional (2D) materials have garnered significant attention in recent years due to their polarization-sensitive photoresponse. However, the inherent crystal structure fundamentally limits the polarization ratio of photocurrent to around 2, which is far below commercial requirements (> 10). Here, the polarimetric photodetector based on vertical asymmetrical 1T' $MoTe_2$/MoS_2/1T' $MoTe_2$ dual van der Waals (vdWs) Schottky junction was demonstrated. Owing to the unique vertical dual-Schottky junction, the device exhibits excellent performance under 915 nm illumination, including a fast rise/decay time of 40/36 μs, a broad 3 dB bandwidth of 12.5 kHz, and ultrahigh polarization ratios of 32 (0.045 V) and 47 (−0.015 V), potentially reaching infinity. Based on the outstanding response speed and polarization sensitivity, the device conveniently achieves polarization angle recognition for linear polarization light by switching external bias voltage without the aid of any polarizer or half-wave plate. In addition, the infrared angle of linear polarization (AoLP) imaging for a target obscured by a blocking film is demonstrated, in which targets with different polarization angles can be clearly distinguished. This work provides a novel scheme for next-generation integrated and all-in-one infrared polarimetric detection and imaging systems.

KEYWORDS: anisotropic, 1T' $MoTe_2$, dual-Schottky junction, all-in-one, polarization detection

1 Introduction

Polarization is a vector characteristic that describes the vibration direction of light waves, which is independent of scalar information such as intensity, wavelength, and phase [1–4]. Polarimetric photodetection technology is essential to the development of optical radar, remote sensing, biological diagnosis, and optical communication devices [5–8]. Compared with traditional intensity detectors, the polarized photodetector can acquire extra polarization states from the target objects and shield stray light, which not only obtains more information but also enhances the capacity to detect and identify the target objects precisely [9, 10]. For the conventional division-of-time, -focal-plane, -amplitude, and -aperture polarimeter structures, drawbacks such as relying on polarizers, complex optical paths, and huge volumes limit the popularization of polarimetric imaging systems [6, 11].

In recent years, emerging anisotropic two-dimensional (2D) materials such as ReS_2, BP, and 1T' $MoTe_2$, with intrinsic polarization-dependent light response, have been regarded as promising active films for integrated and miniaturized polarimetric photodetection [12–15]. Among them, 1T' $MoTe_2$ is an outstanding semimetal possessing high carrier mobility and broad response from deep ultraviolet (UV) to long-wave IR [16]. However, the inherent anisotropic crystal structure fundamentally determines the polarization ratio of photodetectors based on individual materials, which is generally around 2 and not sensitive enough to satisfy the demands of commercial polarized imaging devices [9, 17]. Constructing van der Waals heterojunctions is an effective strategy to modulate the polarization sensitivity [18, 19]. Besides, the built-in electric field in the heterojunction interface can suppress dark current and promote the separation of photo-excited carriers. Thus, the photocurrent and response speed can be effectively improved [20–22].

At present, plenty of van der Waals heterojunction devices based on anisotropic 2D materials such as $MoSe_2$/GeSe/$MoSe_2$ [23],

Received: February 7, 2025; **Revised:** March 7, 2025
Accepted: March 20, 2025

✉Address correspondence to Tielin Shi, tlshi@hust.edu.cn; Bo Sun, bosun@hust.edu.cn

ReS_2/WSe_2 [24], 1T' $MoTe_2/WSe_2$ [18] have been widely explored, showing that the polarization ratio is superior to single anisotropic material. In addition, the gate voltage can regulate the Fermi level of the semiconductor in heterojunctions, which can influence the barrier height and thus modulate the polarization ratio [18, 25, 26]. Nevertheless, these methods either provide a slight improvement in polarization ratio or require additional gates, which complicates the device structure and hinders their industrial applications. On the other hand, the photoresponse of photodetectors based on a single anisotropic 2D material varies cosinusoidally with a 180° period [27–29]. Consequently, the photocurrent and polarization angle do not have a one-to-one correspondence. Each photocurrent value, except for the extrema, corresponds to two polarization angles within a period, rendering the direct identification of the polarization states through photocurrent unfeasible.

Herein, we report a vertically stacked 1T' $MoTe_2/MoS_2$/1T' $MoTe_2$ dual Schottky junction to realize an all-in-one device for angle recognition of linear polarization light. Two back-to-back Schottky junctions ensure that there is always an enhanced built-in field, whether at positive or negative bias, which endows the device with a fast rise/decay time of 40/36 μs and a broad 3 dB bandwidth of 12.5 kHz. We designed the *a*-axis between the top 1T'-$MoTe_2$ and the bottom 1T'-$MoTe_2$ offset by a specific angle, leading to asymmetry photoresponse in the Schottky junctions on both sides of the middle MoS_2. As a result, once a bias is applied to this dual Schottky junction structure under illumination, the photoresponse from one side will be suppressed, and that from another side will dominate, endowing the device with an ultrahigh polarization ratio exceeding 30, potentially reaching infinity. Therefore, we can switch the dominant photoresponse region by altering the external bias voltage, resulting in a unique photocurrent pair corresponding to specific polarization direction. This one-to-one correspondence significantly simplifies the polarization angle recognition for arbitrary linear polarized light. Finally, the infrared AoLP imaging was conducted in obstructed environments without assistance from complex light paths or wave plates, realizing an integrated and miniaturized all-in-one polarimetric system. This work demonstrates a feasible scheme for an on-chip polarization angle recognition photodetector and inspires the design and fabrication of a next-generation polarimetric imaging system with a highly integrated and ultra-compact configuration.

2 Results and discussion

1T' $MoTe_2$ is a novel semimetal 2D material with an in-plane anisotropic crystal structure, which originates from periodic distortion of the lattice and shift of Mo atoms from the corresponding Te octahedron as shown in Fig. S1 in the Electronic Supplementary Material (ESM). The anisotropic crystal structure endows 1T' $MoTe_2$ with anisotropic optical properties. Transmission electron microscopy (TEM) is employed to identify the anisotropic crystal structure of $MoTe_2$. The ribbon-shaped 1T' $MoTe_2$ flake was transferred to a micro-grid copper, as shown in TEM images (Fig. S2 in the ESM). As shown in Fig. 1(a), the high-resolution TEM (HRTEM) image reveals the interplanar spacing of 0.626 and 0.345 nm, which correspond well to the *d*-spacing of (100) and (010) planes [30]. Interestingly, the long side of the ribbon-shaped flake is parallel to the (010) orientation, which means the 1T' $MoTe_2$ crystal is easily cleaved along the *b* axis (Mo-Mo zigzag chain direction), which is similar to 1T' ReS_2 [31]. Furthermore, the inset image in Fig. 1(a) is a select area electron diffraction (SAED) pattern that coincides with the monoclinic structure of the 1T' phase. Angle-resolved polarized Raman (ARPR) is a nondestructive optical method to demonstrate the anisotropic lattice arrangement of the 1T' $MoTe_2$ crystal [26, 32]. Figures 1(b) and 1(c) show the angle-dependent Raman intensity false-color mapping of micromechanical exfoliated 1T' $MoTe_2$ nanosheet under parallel and perpendicular configuration. Herein, the parallel or perpendicular configuration represents the initial polarization direction of the Raman laser parallel or perpendicular

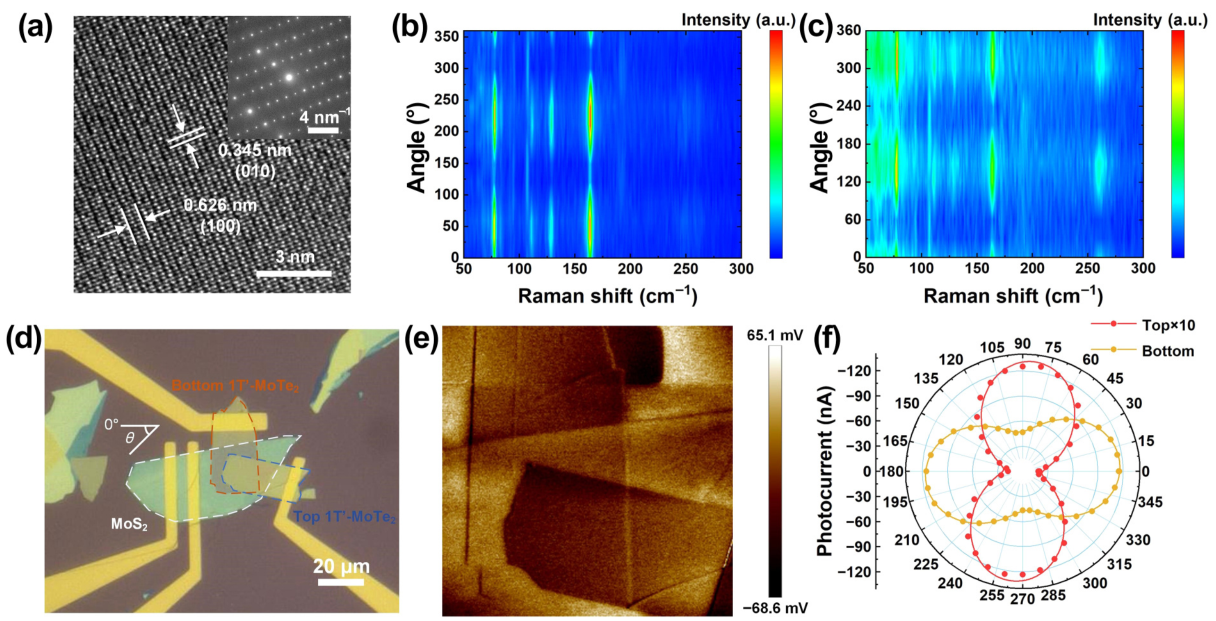

Figure 1 (a) HRTEM image of 1T' $MoTe_2$ flake and SAED image (inset) of the 1T' $MoTe_2$. (b) and (c) The ARPR intensity map of 1T' $MoTe_2$ flake under parallel and perpendicular configuration, respectively. (d) Optical microscopy image of the dual-Schottky junction device with bottom 1T' $MoTe_2$, MoS_2, and top 1T' $MoTe_2$ highlighted by the brown, white, and blue dashed lines, respectively. (e) KPFM image of the 1T'-$MoTe_2/MoS_2$/1T'-$MoTe_2$ heterojunction. (f) Polar plot of photocurrent of bottom 1T'-$MoTe_2/MoS_2$ heterojunction and top 1T'-$MoTe_2/MoS_2$ heterojunction in the device.

清华大学出版社 Tsinghua University Press | SciOpen

to the analyzer direction, denoted as *XX* or *XY*, respectively. It illustrates that the Raman intensity shows strong rotation angle dependence and periodicity, especially for the vibration mode of A_g^1 and A_g^4 at 77.8 and 162.8 cm^{-1}, respectively. To investigate the relationship between the polarization direction and Raman intensity, the polar plots of Raman intensity against polarization angle are plotted (Fig. S3 in the ESM). The maximum Raman intensity appears when the laser polarizes along the (100) crystal orientation in the *XY* configuration. In contrast, in the *XX* configuration, the maximum intensity occurs when the laser polarization direction is along the (010) orientation, which indicates that the crystal orientation can be distinguished by ARPR.

Figure 1(d) shows the optical microscopy image of the dual Schottky junction device. The device consists of a vertically stacked 1T' $MoTe_2$/MoS_2/1T' $MoTe_2$ heterojunction, where the *b*-axis of top 1T' $MoTe_2$ is twisted by an angle (84°) relative to the *b*-axis of bottom $MoTe_2$. The atomic force microscopy (AFM) image of the heterojunction (Fig. S4 in the ESM) shows that the thickness of the bottom $MoTe_2$, middle MoS_2, and top $MoTe_2$ are 62, 8, and 44 nm, respectively. Owing to MoS_2 having a higher Fermi level than that of $MoTe_2$, two Schottky junctions with opposite bending directions are formed in the overlapping region of the tri-layer heterojunction. Figure 1(e) displays the kelvin probe force microscope (KPFM) image of the heterojunction in Fig. 1(d), which can identify the work function difference by measuring the potential difference between the KPFM conducting tip and the sample surface [33, 34]. The work function difference between middle MoS_2 and bottom $MoTe_2$ is calculated to be 26 mV, while that with the top $MoTe_2$ is 51 mV. According to the KPFM result, the energy band alignment before and after contact are plotted (Fig. S5 in the ESM), respectively, where the n-type MoS_2 has a higher Fermi level than that of top/bottom 1T' $MoTe_2$. Upon contact, two depletion regions with opposite built-in electric field directions are formed. We measured the *I*–*V* curves of the bottom and top Schottky junctions (Fig. S6 in the ESM), respectively, and both have apparent rectification characteristics, which further proves the existence of dual Schottky barriers. As shown in Fig. 1(f), the behavior of the bottom and top Schottky junction in the tri-layer structure is consistent with bilayer 1T' $MoTe_2$/MoS_2 heterojunction, and they all show polarized photoresponse with a period of 180°. Moreover, the maximum photocurrent occurs when the polarized direction is perpendicular to the ribbon-shaped 1T' $MoTe_2$ flake. According to HRTEM and ARPR test results, the maximum photocurrent in 1T' $MoTe_2$/MoS_2 heterojunction appears when the excitation light is polarized vertically to the *b*-axis. The photoresponse can be fitted by a cosine function as [7, 11, 12]

$$I_{ph} = I_{max}\cos^2(\theta+\varphi) + I_{min}\sin^2(\theta+\varphi) \quad (1)$$

where θ, φ, I_{max}, and I_{min} are the rotation angle of the laser polarization direction, the offset phase angle between the initial laser polarization direction and the *a*-axis of 1T' $MoTe_2$ flakes, the maximum value of photocurrent, and the minimum value of the photocurrent, respectively.

Further, we illustrate the energy band diagram of the tri-layer heterojunction with bias applied in Figs. 2(a) and 2(b). By applying a positive voltage (top to bottom), the Fermi level of the top 1T'-$MoTe_2$ shifted downward, the top junction was under forward bias, while the bottom junction was under reverse bias. When the heterojunction is under illumination, both the top junction and the bottom junction can generate photogenerated carriers. In the bottom junction, the photogenerated electron-hole pairs can be separated and drifted to the electrodes. However, the energy band bending in the top junction forms a blocking layer for holes, which can result in the accumulation of holes and the recombination of photogenerated electron-hole pairs [11]. In the dual-Schottky junction system, the reverse-biased junction dominates the device's photocurrent contribution. Figure 2(c) shows the *I*–*V* curves under 915 nm illumination with the incident polarization direction along the *a*-axis of bottom 1T' $MoTe_2$ and the top 1T' $MoTe_2$, respectively, where the incident power is swept from 0 to 124.23 μW. It is evident that the photocurrent can be modulated by both the intensity and the polarization direction of the incident light. Combining the energy band diagram and *I*–*V* curves, we can divide the photoresponse into three parts: part I (V_{ds} > 0.045 V), part II (V_{ds} < –0.015 V), and part III (–0.015 V < V_{ds} < 0.045 V). In part I, the bottom junction is under reverse bias, which dominates the photoresponse. Although the polarization direction of light is along the *a*-axis of top 1T' $MoTe_2$, almost no photocurrent is generated (blue lines in Fig. 2(c)). Once the polarization direction is adjusted along the *a*-axis of bottom 1T' $MoTe_2$ (red lines in Fig. 2(c)), the photocurrent continuously increases with increasing incident power. In contrast, the photocurrent behaves inversely in part II. In part III, neither the bottom junction nor the top junction holds an absolute advantage, and both contribute to the photocurrent. This means that the polarization direction will affect the flow direction of the photocurrent, enabling a transition of photocurrent from positive to negative, which is inexistent in ordinary polarization-sensitive devices [35–37].

The time-resolved photoresponse at –0.015 and 0.045 V bias is displayed in Figs. 2(d) and 2(e), respectively, in which the device is illuminated under switching light with intensity corresponding to Fig. 2(c). The photoresponse is stable and repeatable under various light intensities. We extracted the photocurrent as a function of laser power on a logarithmic scale in Fig. 2(f). The photocurrent at both biases can both be fitted by $I \propto P^\alpha$ [38–40], and the fitting parameter α is calculated to be 0.92 and 0.96, respectively, indicating the excellent linearity of the photoresponse.

Figure 2(g) shows the *I*–*V* curves at various laser polarization angles. When the V_{ds} are between –0.015 and 0.045 V, the I_{ds} appear bipolarity as the rotation of the polarization angle. The 1T' $MoTe_2$ exhibits strong inherent in-plane optical anisotropy. The difference in the direction of the *a*-axis of top and bottom 1T' $MoTe_2$ results in different optical absorption; thus, the photocarriers in the top and bottom 1T' $MoTe_2$ compete to form the photocurrent [41]. In brief, the I_{ds} in the dual Schottky junction is the result of competition between the bottom junction photocarriers and top junction photocarriers. When the laser polarized approach to the *a*-axis of the bottom $MoTe_2$, even under negative voltage, the photocurrent is still positive. In contrast, when the laser polarized approach to the *a*-axis of the top $MoTe_2$, even under positive voltage, the photocurrent is still negative.

Figure S7 in the ESM depicts the transient response of the dual-Schottky device to switching laser with frequencies of 50 Hz, 1 kHz, 5 kHz, and 12.5 kHz, respectively. It can be observed that the response is fast and stable at low frequency but degrades at high frequency. A switching period response curve at 1 kHz with steep rise and decay edges is presented in Fig. 2(h) to evaluate the response speed, which is the time intervals of photocurrent rise from 10% to 90% (τ_{rise}) and decay from 90% to 10% (τ_{decay}) of maximum [42–44]. It is noted that the rise/decay time is as fast as

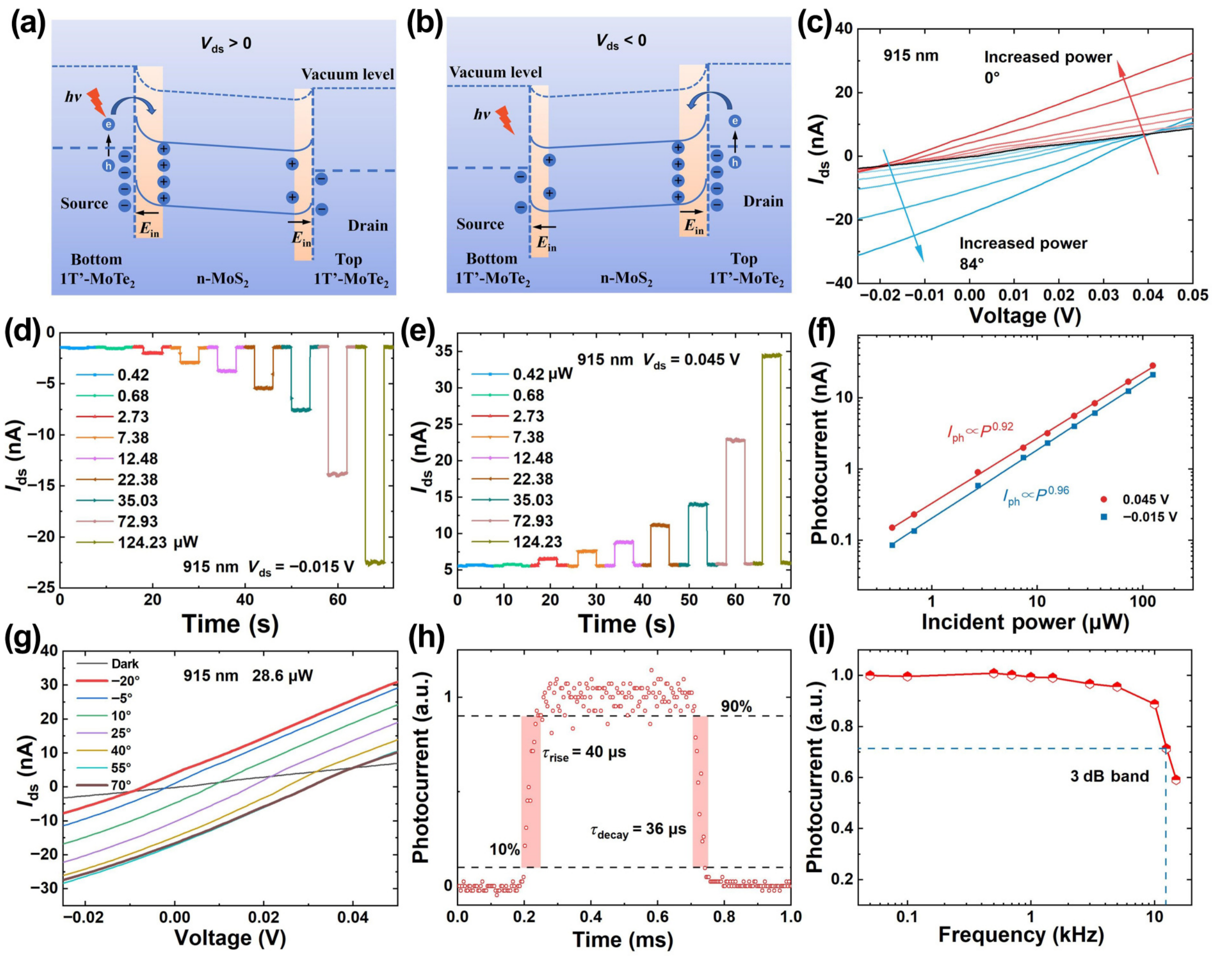

Figure 2 Optoelectronic performance of 1T'-$MoTe_2$/MoS_2/1T'-$MoTe_2$ dual-Schottky junction device under 915 nm light illumination. (a) and (b) Energy band alignments of the device in the case of $V_{ds} > 0$ and $V_{ds} < 0$, respectively. (c) *I*–*V* characteristics of the device under various light illumination powers. The red curves represent light incident polarizes along the *a*-axis of bottom 1T' $MoTe_2$ and the blue curves represent light incident polarizes along the *a*-axis of top1T' $MoTe_2$. (d) and (e) Time-resolved photoresponse of the device under various light illumination powers at −0.015 V bias and 0.045 V bias, respectively. (f) Photocurrent as a function of incident power at −0.015 V bias with an incident polarization angle of 0° and 0.045 V bias with an incident polarization angle of 90°. (g) *I*–*V* characteristics of the device at various laser polarization angles. (h) Rise and decay time of a temporal response cycle at the frequency of 1 kHz. (i) 3 dB band test of the device.

40/36 μs, superior to other 2D materials photodetectors [14, 23, 41]. Figure 2(i) shows the normalized photocurrent of the device as a function of frequency (from 50 Hz to 15 kHz). The 3 dB frequency was estimated to be 12.5 kHz, suggesting that the dual-Schottky junction device is capable of detecting ultrafast optical signals.

Based on the excellent and stable optical performance of the device, the polarization-sensitive detection of the device was investigated. The light passes through a Glan-Taylor prism, a half-wave plate, and then strikes the tri-overlapping region of the device in the measurement setup (Fig. S8 in the ESM). Figures 3(a) and 3(d) give the time-resolved photoresponse curves with varying polarization angles of the dual Schottky junction device at −0.015 and 0.045 V bias, respectively. The amplitude of the photocurrent changes periodically with polarized angles. The photocurrent polarization ratios, defined as the peak-to-valley ratio $(I_{max} - I_{dark})/(I_{min} - I_{dark})$ [45–47], are as high as 32 and 47 for 0.045 V bias and −0.015 V bias, respectively, which is significantly improved compared with 1T' $MoTe_2$/MoS_2 heterojunction [35]. To further confirm the photocurrent generation mechanism of the tri-layer region, spatial polarization photocurrent mapping of the dual-Schottky junction device at different voltage and laser polarization directions are investigated. During the scanning, the 915 nm laser was focused by a 50 × objective (NA = 0.5) to be a 3 μm spot and scanned at a 0.5 μm step. The photocurrent mapping of the device at V_{ds} = −0.015 V bias with laser polarize along photocurrent maximum angle and minimum angle is shown in Figs. 3(b) and 3(c), respectively. The photocurrent generation region can be divided into three sections, including a tri-overlapping region formed by 1T' $MoTe_2$/MoS_2/1T' $MoTe_2$ heterojunction (region I) and two bi-overlapping regions formed by the middle MoS_2 with the top and bottom 1T' $MoTe_2$, respectively (regions II and III). The photocurrent mapping of region I is consistent with the *I*–*V* characteristic of the dual Schottky junction device. Under negative voltage, region II is at reverse bias while region III is at forward bias, resulting in a superior photoresponse in region II compared to region III. The photocurrent in region III is positive and exhibits a larger value at the polarization angle of −35°, whereas the photocurrent in region II is negative and shows a larger value at the polarization angle of 55°. The photocurrent in region I behaves similarly to that in region II, indicating the reverse-biased top Schottky junction dominates the photoresponse of region I. At 0.045 V bias, the photocurrent in the tri-overlapping region

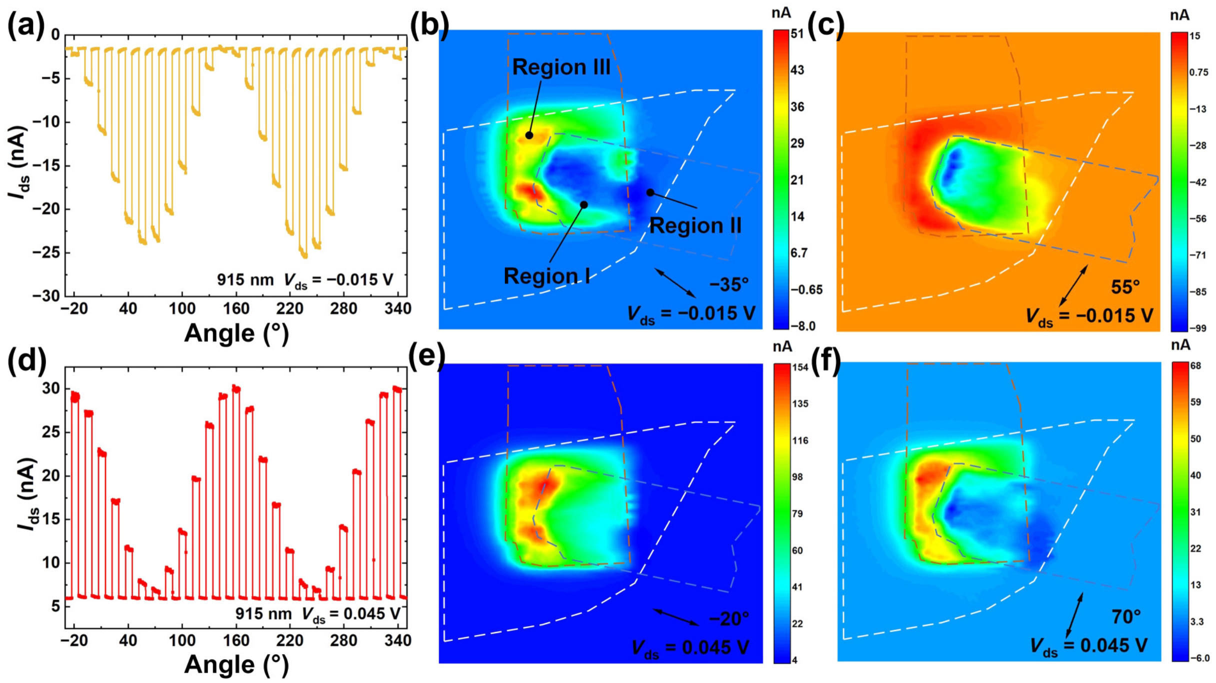

Figure 3 (a) Time-dependent photoresponse by varying polarization angles at V_{ds} of −0.015 V under 915 nm light illumination. (b) and (c) Photocurrent mapping with −35° and 55° polarization angle of 915 nm scanning laser at V_{ds} of −0.015 V. (d) Time-dependent photoresponse by varying polarization angles at V_{ds} of 0.045 V under 915 nm light illumination. (e) and (f) photocurrent mapping with −20° and 70° polarization angle of 915 nm scanning laser at V_{ds} of 0.045 V.

experiences a remarkable tens-of-fold increase when the polarization direction of the scanning laser is rotated to be closer to the *a*-axis of the bottom 1T' $MoTe_2$ (Figs. 3(e) and 3(f)), demonstrating the bottom Schottky junction dominates the photocurrent generation. It is noteworthy that, regardless of whether a positive or negative voltage is applied, there will always be one junction in reverse bias and another in forward bias in the tri-overlapping dual-Schottky junction region. Due to its stronger built-in electric field, the reverse-biased Schottky junction dominates the photoresponse. However, the forward-biased junction still generates a small amount of photogenerated carriers. Thus, the photocurrent in the dual-Schottky junction region results from competition between photogenerated carriers from the reverse-biased and forward-biased regions under polarization light.

The contour plot of the polarization angle-dependent photocurrent at V_{ds} from −0.1 to 0.1 V is depicted in Fig. 4(a). It is obvious that the photocurrent changes periodically with the change of polarization angle under various bias voltages. In Fig. 4(b), the polarization ratio is calculated as a function of V_{ds}. The results show that the polarization ratio around −0.015 and 0.045 V has a sharp increase, approaching positive or negative infinity. Since the photogenerated carriers from the bottom Schottky junction and the top Schottky junction compete to form the photocurrent, the increase of photogenerated carriers on the non-dominant side will inhibit the photocurrent, resulting in a decrease of I_{min} and a dramatic increase of polarization ratio. Figure 4(c) presents the performance comparison of our device with the latest reported anisotropic 2D material-based polarization sensitive photodetectors in terms of polarization ratio and response speed. Our device demonstrates superior polarization ratio and response speed, which holds great promise for application in highly integrated and ultra-compact polarimetric imaging system.

To demonstrate the capacity for linear polarized angle recognition, the polar plots of angle-resolved photocurrent under 915 nm illumination with switching bias corresponding to Figs. 3(a) and 3(d) are shown in Fig. 4(d). The relationship between photocurrent and linear polarized angle can be fitted by Eq. (1) as well. Compared with Fig. 1(f), it can be found that in the tri-overlapping region the maximum photocurrent direction is offset by 25° from the *a*-axis of bottom/top 1T' $MoTe_2$ at 0.045 V/ −0.015 V bias and the phase difference $\Delta\varphi$ of the fitting equation for 0.045 V and −0.015 V is about 84° which is consistent with the offset angle between *a*-axis of bottom and top 1T' $MoTe_2$. Here, we define the photocurrent at −0.015 V bias as I_{ph1} and the photocurrent at 0.045 V bias as I_{ph2}. Both I_{ph1} and I_{ph2} exhibit a 180° periodic cosine relationship with polarization angle. For I_{ph1}, any current value situated between maximum and minimum corresponds to two distinct angles within one period, which makes it difficult to distinguish the exact linear polarized angle. However, on account of the phase offset of I_{ph1} and I_{ph2}, the two distinct polarized angles correspond to two different photocurrent values of I_{ph2}. Therefore, we can calculate the possible polarized direction using I_{ph1} and then measure the I_{ph2} to determine the specific polarized angle. We plot the path of point (I_{ph1}, I_{ph2}) in Fig. 4(e) where every point represents a polarized angle. Considering that I_{ph1} and I_{ph2} are in the form of cosine, the fitting functions of I_{ph1} and I_{ph2} can be regarded as parametric equations for an ellipse. Thus, the track of (I_{ph1}, I_{ph2}) is an ellipse, which we call the polarimetry ellipse. The ellipse is inscribed within a rectangle formed by extreme values of I_{ph2} and I_{ph1}. The rotation angle β of the polarimetry ellipse can be calculated by

$$\tan 2\beta = \frac{2A_1A_2\cos(2\Delta\varphi)}{A_2^{\ 2} - A_1^{\ 2}} \tag{2}$$

where A_1 and A_2 are the amplitudes of I_{ph1} and I_{ph2} fitted curves, respectively, and $\Delta\varphi$ is the phase offset of I_{ph1} and I_{ph2} (Fig. S9 in the ESM for details). Regardless of the values of A_1 and A_2, when $\Delta\varphi$

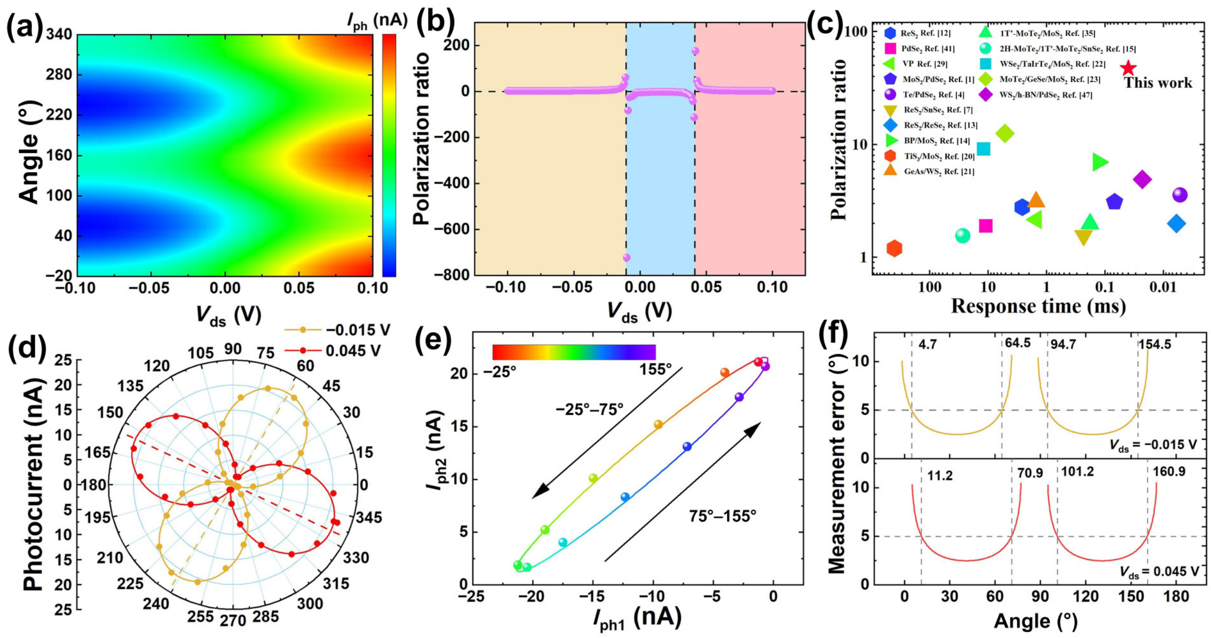

Figure 4 (a) 2D contour plot of photocurrent distribution as a function of polarized angles and V_{ds}. (b) Calculated polarization ratio as a function of V_{ds}. (c) Comparison of the response speed and polarization ratio of the 1T'-$MoTe_2$/MoS_2/1T'-$MoTe_2$ device with other polarization-sensitive all-2D photodetectors (ReS_2 [12], $PdSe_2$ [41], Violet phosphorus [29], MoS_2/$PdSe_2$ [1], Te/Pde_2 [4], ReS_2/$SnSe_2$ [7], ReS_2/$ReSe_2$ [13], BP/MoS_2 [14], TiS_3/MoS_2 [20], GeAs/WS_2 [21], 1T'-$MoTe_2$/MoS_2 [35], 2H-$MoTe_2$/1T'-$MoTe_2$/$SnSe_2$ [15], WSe_2/$TaIrTe_4$/MoS_2 [22], $MoTe_2$/GeSe/MoS_2 [23], WS_2/h-BN/$PdSe_2$ [47]). (d) Polar plot of the polarization angle dependent photocurrent of the device at positive and negative bias. (e) The polarimetry ellipse obtained by plotting the photocurrent point (I_{ph1}, I_{ph2}) in a coordinate system, in which every point replaces a polarization angle of incident light in the range of 0 to 180°. (f) Measurement error as a function of polarization angles when the current fluctuation is ±0.5 nA.

= 45°, β = 0°, thus the polarimetry ellipse is a standard ellipse that has not been rotated. In particular, the polarimetry ellipse degenerates into the diagonal of the rectangle when $\Delta\varphi$ = 0° or 90°.

Subsequently, we investigate the angle measurement error by the polarimetry ellipse. When calculating the polarized angle θ using the photocurrent according to Eq. (1), a significant drawback emerges around the extreme values of the photocurrent, where even minor fluctuations in the current can lead to large changes in the computed θ. Assuming that the current fluctuation is ±0.5 nA, the measurement errors of Device1 are plotted in Fig. 4(f), in which the measurement error is defined as the difference of theta calculated by the fluctuated current. We define the range of source angle with measurement errors within 5° as the confidence interval. The centers of the confidence interval under positive and negative bias will shift according to the phase offset of the photocurrent.

We designed the dual Schottky device with different configurations, including the *a*-axis of bottom and top 1T' $MoTe_2$ with 67° (defined as Device2) and 90° (defined as Device3) offset angles, and the corresponding optical microscopy images are shown in Fig. S10 in the ESM. The time-resolved I_{ds} at positive bias and negative bias of Device2 and Device3 are shown in Fig. S11 in the ESM. The photoresponse is steep and stable with a period of 180°. The photocurrent mapping results of Device2 and Device3 are consistent with those of Device1 (Figs. S12 and S13 in the ESM). This has further proved that the top Schottky junction dominates the photoresponse of the device under negative bias, while the bottom heterojunction dominates when a positive bias is applied. The corresponding polar photocurrents are plotted in Fig. S14 in the ESM, where the phase offsets all correspond to the angles between the *a*-axes. The bias-switched polarization angle recognition by polarimetry ellipse is also verified in Fig. S15 in the ESM. The polarimetry ellipse shape and rotation angle of Device2 are significantly different from Device1 due to the differences in photocurrent extrema and the angle between the *a*-axis of the top and bottom 1T' $MoTe_2$. But for Device3, the phase offset is 90°, and the path of the experimentally measured (I_{ph1}, I_{ph2}) is well fitted by a line with a slope of A_1/A_2, which accords with the calculation of Eq. (2).

Based on the excellent photodetection performance and bias-switched polarization direction recognition of the dual Schottky junction device, the polarization imaging capability is demonstrated by a single-point sensing pixel imaging experiment. Figure 5(a) illustrates the schematic diagram of the setup, where the linearly polarized light sequentially passes through a hollow mask and a halfwave plate and then is focused on the device by a 50× objective. In the polarization imaging system, the mask acts as an imaging object and target objects with different polarization angles can be simulated by adjusting the angle of the halfwave plate. Compared with visible light, infrared polarized light has stronger penetration capability. Therefore, infrared polarization imaging is more advantageous in some complex environments. We put a shading film between the mask and the half-wave plate to simulate the blocking from the environment. Figure 5(b) shows the photocurrent mapping results under 0°, 45°, 90°, and 135° polarization angle illumination at 0.045 V positive and −0.015 V negative biases. Although the mask is blocked, both mapping images show clear borders.

Subsequently, the AoLP mapping was calculated in Fig. 5(c), in which the polarized angles of letters in the hollow mask can be recognized directly and accurately. This all-in-one design allows the device to obtain the AoLP of light by switching the bias voltage only once, revealing its great potential in filter-less infrared polarization imaging.

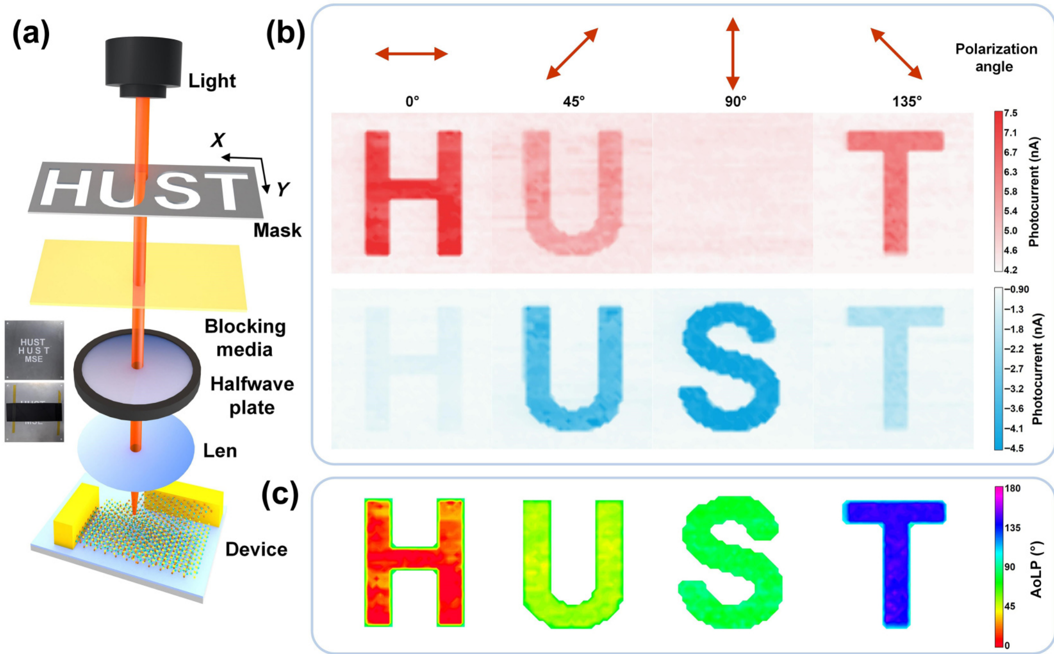

Figure 5 (a) Schematic of the test setup for photocurrent imaging and AoLP imaging. (b)The photocurrent imaging of the mask of H, U, S, and T letters with polarization angles of 0°, 45°, 90°, and 135°, respectively. (c) The calculated AoLP image of the mask, from which the polarized angle of the target object can be identified directly.

3 Conclusions

In summary, we have demonstrated a dual vdWs Schottky junction device composed of vertically stacked 1T' $MoTe_2$/MoS_2/1T' $MoTe_2$ heterojunction, in which the middle MoS_2 forms two back-to-back Schottky barriers with the bottom and top 1T' $MoTe_2$. The device exhibits fast photoresponse and high polarization sensitivity under 915 nm laser illumination, including a fast rise/decay time of 40/36 μs, −3 dB cutoff frequency of 12.5 kHz, and ultrahigh polarization ratio of 32 and 47. Through meticulous asymmetrical design, the *a*-axis of the bottom and top 1T' $MoTe_2$ is offset by a certain angle, allowing the device to identify the polarization angle of incident linear polarization light by simply switching the voltage direction once, without any assistance from polarizers or half-wave plates. More importantly, the AoLP imaging is successfully realized by simulating targets with different polarization angles. The novel 1T' $MoTe_2$/MoS_2/1T' $MoTe_2$ dual Schottky junction will provide a promising scheme for the design and fabrication of the next-generation on-chip polarimetric system.

4 Experimental section

4.1 Device fabrication

The semimetal 1T'-$MoTe_2$ and 2H-MoS_2 flakes were all mechanically exfoliated onto 300 nm thick SiO_2/Si substrates using polydimethylsiloxane (PDMS) from single crystal bulks, purchased from Shenzhen six Carbon Technology Co., Ltd. Then ribbon-shaped 1T'-$MoTe_2$ flakes were carefully selected to construct the tri-layer heterojunction with MoS_2 by the polyvinyl alcohol (PVA) wetting transfer method. PVA aqueous solution with a 5% mass fraction was spin-coated on glass, forming a transparent film, and then the film was cut and placed on PDMS. The PVA/PDMS composite film was loaded on a 2D materials transfer stage to transfer the bottom 1T' $MoTe_2$, middle MoS_2, and top 1T' $MoTe_2$ to the target area sequentially. Finally, the electrodes of the bottom and top 1T' $MoTe_2$ were fabricated by a standard lift-off process, in which maskless direct writing photolithography system (MicroLab III, SVG TECH GROUP) and electron beam evaporation were implemented to deposit Cr/Au (8/40 nm) electrodes.

4.2 Characterization and measurement

Ultra-depth three-dimensional microscope (Keyence VHX-1000) was used to record the optical image of 1T' $MoTe_2$ flakes and dual Schottky heterojunction devices. Angle-resolved polarized Raman spectral was measured by a confocal Raman microscope (LabRAM HR Evolution HORIBA Jobin Yvon, laser excitation of 532 nm). Lattice structure and selected area electron diffraction of 1T' $MoTe_2$ flakes were obtained by field emission transmission electron microscopy (FETEM, Tecnai G2 F30, FEI). The thickness and potential of the sample were extracted by a KPFM (Dimension FastScan from Bruker Co., Ltd) with a conductive tip. The spatial mapping of the photocurrent was obtained by photocurrent measuring instruments (Xper-PC, Nanobase, Inc). The light sources were all single-mode lasers (915nm) driven by laser diode controller (ITC 4001, Thorlabs), and the light intensity was monitored by optical power meter kits (PM100D, Thorlabs). The photoelectric properties of the device were collected by Keithley 2636B digital source meter on a four-probe station (SCG-O-2, Semishare Co., Ltd) on a damped vibration isolation optical platform (HGZZ0906Z Wuhan Red Star Yang Science and Technology Co., Ltd) under 915 nm laser illumination. A digital oscilloscope (Tektronix, TDS2012B) was employed to record the transient photoresponse of the device under different switching frequencies. All the tests were conducted in ambient conditions.

Electronic Supplementary Material: Supplementary material (crystal structures, optical microscope image, TEM images, and Raman data of 1T' $MoTe_2$; AFM images and energy band alignment of the 1T'-$MoTe_2$/MoS_2/1T'-$MoTe_2$ heterojunction; rectify characteristic of 1T' $MoTe_2$/MoS_2 heterojunction; photoresponse properties and measurement setup of the 1T'-$MoTe_2$/MoS_2/1T'-$MoTe_2$ heterojunction; photocurrent and polarimetry ellipse evolution at different $\Delta\varphi$; optical microscope images, time-dependent photoresponse, photocurrent mapping, polar plot of the polarization angle dependent photocurrent, and polarimetry ellipse of Device2 and Device3) is available in the online version of this article at https://doi.org/10.26599/NR.2025.94907392.

Data availability

All data needed to support the conclusions in the paper are presented in the manuscript and the Electronic Supplementary Material. Additional data related to this paper may be requested from the corresponding author upon request.

Acknowledgements

The authors acknowledge the financial support from the National Natural Science Foundation of China (No. 52075207), the Fundamental Research Funds for the Central Universities (No. YCJJ20241102), and the Shenzhen Science and Technology Program (No. JCYJ20240813153431041). The authors thank the Analytical and Testing Center of Huazhong University of Science and Technology (HUST) for TEM and Raman measurements. The authors also thank the Optoelectronic Micro&Nano Fabrication and Charactering Facility of Wuhan National Laboratory for Optoelectronics for ultraviolet maskless photolithography.

Declaration of competing interest

All the contributing authors report no conflict of interests in this work.

Author contribution statement

L. X. K.: Conceptualizaition, experimental design, data curation, visualization, writing-original draft, funding acquisition. Q. S.: Formal analysis, investigation, methodology. S. J. W.: Experimental design, investigation, methodology. Z. Y. L.: Resources, validation, supervision. G. L. L.: Project administration, resources, supervision. B. S.: Methodology, validation, funding acquisition, resources, supervision, writing – review & editing. T. L. S.: Methodology, validation, funding acquisition, resources, supervision, writing – review & editing.

Use of AI statement

None.

References

[1] Yin, C. D.; He, S. X.; Fan, X. F.; Xiao, Y. K.; Zhao, L. C.; Gao, L. M. Gate-modulated and polarization-sensitive photodetector based on the MoS_2/$PdSe_2$ out-of-plane van der Waals heterostructure. *Adv. Opt. Mater.* **2024**, *12*, 2401122.

[2] Wei, J. X.; Xu, C.; Dong, B. W.; Qiu, C. W.; Lee, C. Mid-infrared semimetal polarization detectors with configurable polarity transition. *Nat. Photonics* **2021**, *15*, 614–621.

[3] Wu, D.; Xu, M. M.; Zeng, L. H.; Shi, Z. F.; Tian, Y. Z.; Li, X. J.; Shan, C. X.; Jie, J. S. *In situ* fabrication of $PdSe_2$/GaN Schottky junction for polarization-sensitive ultraviolet photodetection with high dichroic ratio. *ACS Nano* **2022**, *16*, 5545–5555.

[4] Wang, P.; Li, Z.; Xia, X.; Zhang, J. N.; Lan, Y. Y.; Zhu, L.; Ke, Q. Q.; Mu, H. R.; Lin, S. H. Anisotropic Te/$PdSe_2$ van der Waals heterojunction for self-powered broadband and polarization-sensitive photodetection. *Small* **2024**, *20*, 2401216.

[5] Xin, W.; Zhong, W. H.; Shi, Y. J.; Shi, Y. M.; Jing, J. W.; Xu, T. F.; Guo, J. X.; Liu, W. Z.; Li, Y. Z.; Liang, Z. Z. et al. Low-dimensional-materials-based photodetectors for next-generation polarized detection and imaging. *Adv. Mater.* **2024**, *36*, 2306772.

[6] Tong, L.; Huang, X. Y.; Wang, P.; Ye, L.; Peng, M.; An, L. C.; Sun, Q. D.; Zhang, Y.; Yang, G. M.; Li, Z. et al. Stable mid-infrared polarization imaging based on quasi-2D tellurium at room temperature. *Nat. Commun.* **2020**, *11*, 2308.

[7] Fu, Z. Y.; Han, J. Y.; Wei, L. J.; Wei, Y. C.; Huo, X. H.; Li, C. Y.; Xie, J. L.; Zhou, H. X.; Yu, H.; Gou, J. et al. Polarization-sensitive self-powered photodetector based on anisotropic/isotropic ReS_2/$SnSe_2$ van der Waals heterojunction. *Adv. Opt. Mater.* **2024**, *12*, 2401306.

[8] Li, L. N.; Liu, X. T.; Li, Y. B.; Xu, Z. Y.; Wu, Z. Y.; Han, S. G.; Tao, K. W.; Hong, M. C.; Luo, J. H.; Sun, Z. H. Two-dimensional hybrid perovskite-type ferroelectric for highly polarization-sensitive shortwave photodetection. *J. Am. Chem. Soc.* **2019**, *141*, 2623–2629.

[9] Zhang, J. B.; Zhou, N.; Zhang, L. H.; Shang, C. H.; Li, J. X.; Zhao, Y.; Jia, G. H.; Yang, R. S.; Xu, H.; Li, X. B. Optical and electrical anisotropy regulation engineering of low-dimensional materials toward polarized detection and imaging applications. *Rare Met.* **2024**, *43*, 2968–2993.

[10] Han, Z. Y.; Fu, W. F.; Zou, Y. S.; Gu, Y.; Liu, J. X.; Huang, B.; Yu, D. J.; Cao, F.; Li, X. M.; Xu, X. B. et al. Oriented perovskite growth regulation enables sensitive broadband detection and imaging of polarized photons covering 300–1050 nm. *Adv. Mater.* **2021**, *33*, 2003852.

[11] Deng, W. J.; Dai, M. J.; Wang, C. W.; You, C. Y.; Chen, W. D.; Han, S.; Han, J. Y.; Wang, F. K.; Ye, M.; Zhu, S. et al. Switchable unipolar-barrier van der Waals heterostructures with natural anisotropy for full linear polarimetry detection. *Adv. Mater.* **2022**, *34*, 2203766.

[12] Hu, Y. B.; He, J. J.; Yan, Z. Y.; Xu, C.; Li, X. B.; Wei, N.; Wang, Y.; Dong, N. N.; Wang, J. High performance balanced linear polarization photodetector based on 2D ReS_2. *Laser Photon. Rev.* **2024**, *18*, 2400661.

[13] Li, K. L.; Du, C. H.; Gao, H. L.; Yin, T. H.; Zheng, L. Y.; Leng, J. C.; Wang, W. J. Ultrafast and polarization-sensitive ReS_2/$ReSe_2$ heterostructure photodetectors with ambipolar photoresponse. *ACS Appl. Mater. Interfaces* **2022**, *14*, 33589–33597.

[14] Liu, C.; Ding, S. M.; Tian, Q. L.; Hong, X. T.; Su, W. H.; Tang, L.; Wang, L. M.; Zhang, M. L.; Liu, X. Q.; Lv, Y. W. et al. Realizing the switching of optoelectronic memory and ultrafast detector in functionalized-black phosphorus/MoS_2 heterojunction. *Laser Photon. Rev.* **2023**, *17*, 2200486.

[15] Sun, Y. M.; Xiong, J. X.; Wu, X. M.; Gao, W.; Huo, N. J.; Li, J. B. Highly sensitive infrared polarized photodetector enabled by out-of-plane PSN architecture composing of p-$MoTe_2$, semimetal-$MoTe_2$ and n-$SnSe_2$. *Nano Res.* **2022**, *15*, 5384–5391.

[16] Wu, D.; Guo, C. G.; Zeng, L. H.; Ren, X. Y.; Shi, Z. F.; Wen, L.; Chen, Q.; Zhang, M.; Li, X. J.; Shan, C. X. et al. Phase-controlled van der Waals growth of wafer-scale 2D $MoTe_2$ layers for integrated high-sensitivity broadband infrared photodetection. *Light: Sci. Appl.* **2023**, *12*, 5.

[17] Zhou, Z. Q.; Shen, T.; Wang, P.; Guo, Q. L.; Wang, Q. H.; Ma, C. J.; Xin, K. Y.; Zhao, K.; Yu, Y. L.; Qin, B. et al. Low symmetric sub-wavelength array enhanced lensless polarization-sensitivity photodetector of germanium selenium. *Sci. Bull.* **2023**, *68*, 173–179.

[18] Wang, H. Y.; Li, Y.; Gao, P.; Wang, J. N.; Meng, X. F.; Hu, Y.; Yang, J. H.; Huang, Z. H.; Gao, W.; Zheng, Z. Q. et al. Polarization- and gate-tunable optoelectronic reverse in 2D semimetal/semiconductor photovoltaic heterostructure. *Adv. Mater.* **2024**, *36*, 2309371.

[19] Wan, P.; Jiang, M. M.; Wei, Y.; Xu, T.; Liu, Y.; Xia, S. H.; Su, L. X.; Shi, D. N.; Fang, X. S.; Kan, C. X. Junction-enhanced polarization sensitivity in self-powered near-infrared photodetectors based on Sb_2Se_3 microbelt/n-GaN heterojunction. *Adv. Opt. Mater.* **2023**, *11*, 2202080.

[20] Lv, T.; Huang, X. Y.; Zhang, W. G.; Deng, C. S.; Chen, F. Y.; Wang, Y. C.; Long, J.; Gao, H.; Deng, L. M.; Ye, L. et al. High-responsivity multiband and polarization-sensitive photodetector based on the TiS_3/MoS_2 heterojunction. *ACS Appl. Mater. Interfaces* **2022**, *14*, 48812–48820.

[21] Xiong, J. X.; Dan, Z. Y.; Li, H. Y.; Li, S. N.; Sun, Y. M.; Gao, W.; Huo, N. J.; Li, J. B. Multifunctional GeAs/WS_2 heterojunctions for highly polarization-sensitive photodetectors in the short-wave infrared range. *ACS Appl. Mater. Interfaces* **2022**, *14*, 22607–22614.

[22] Han, X. N.; Wen, P. T.; Zhang, L.; Gao, W.; Chen, H. Y.; Gao, F.; Zhang, S. H.; Huo, N. J.; Zou, B. S.; Li, J. B. A polarization-sensitive self-powered photodetector based on a p-$WSe_2/TaIrTe_4$/n-MoS_2 van der Waals heterojunction. *ACS Appl. Mater. Interfaces* **2021**, *13*, 61544–61554.

[23] An, K.; Pan, Y.; Rong, X. M.; Zheng, T.; Li, L.; Sun, H. R.; Zeng, J.; Sang, Y. H.; Huang, F. Y.; Yue, D. W. et al. High-performance self-driven polarization-sensitive imaging photodetectors based on fully depleted T-$MoSe_2$/GeSe/b-$MoSe_2$ van der Waals dual-heterojunction. *Adv. Funct. Mater.* **2024**, *34*, 2409331.

[24] Wu, W. L.; Liu, Z. Y.; Qiu, Z. C.; Wu, Z. Q.; Li, Z. M.; Yang, X.; Han, L. X.; Li, C. Y.; Huo, N. J.; Wang, X. Z. et al. An ultrasensitive $ReSe_2/WSe_2$ heterojunction photodetector enabled by gate modulation and its development in polarization state identification. *Adv. Opt. Mater.* **2024**, *12*, 2301410.

[25] Shen, D. Z.; Yang, H.; Patel, T.; Rhodes, D. A.; Timusk, T.; Zhou, Y. N.; Kim, N. Y.; Tsen, A. W. Gate-tunable multiband van der Waals photodetector and polarization sensor. *ACS Nano* **2024**, *18*, 11193–11199.

[26] Zhang, L.; Han, X. N.; Zhang, S. H.; Wang, H. Y.; Huang, Y.; Zheng, Z. Q.; Huo, N. J.; Gao, W.; Li, J. B. Gate-tunable photovoltaic behavior and polarized image sensor based on all-2D $TaIrTe_4/MoS_2$ van der Waals Schottky diode. *Adv. Electron. Mater.* **2022**, *8*, 2200551.

[27] Du, X.; Wu, H. J.; Peng, Z. H.; Tan, C.; Yang, L.; Wang, Z. G. Room-temperature polarization-sensitive photodetectors: Materials, device physics, and applications. *Mater. Sci. Eng.: R: Rep.* **2024**, *161*, 100839.

[28] Wu, D.; Guo, J. W.; Du, J.; Xia, C. X.; Zeng, L. H.; Tian, Y. Z.; Shi, Z. F.; Tian, Y. T.; Li, X. J.; Tsang, Y. H. et al. Highly polarization-sensitive, broadband, self-powered photodetector based on graphene/$PdSe_2$/germanium heterojunction. *ACS Nano* **2019**, *13*, 9907–9917.

[29] Chen, W. L.; Chen, A.; Zhang, R.; Zeng, J. M.; Zhang, L. H.; Gu, M. Y.; Wang, C. F.; Huang, M. Y.; Guo, Y. B.; Duan, H. X. et al. Strong in-plane optoelectronic anisotropy and polarization sensitivity in low-symmetry 2D violet phosphorus. *Nano Lett.* **2023**, *23*, 10821–10831.

[30] Wang, X. J.; Shang, J.; Zhu, M. J.; Zhou, X.; Hao, R.; Sun, L. N.; Xu, H.; Zheng, J. B.; Lei, X. F.; Li, C. et al. Controlled growth of large-scale uniform 1T′ $MoTe_2$ crystals with tunable thickness and their photodetector applications. *Nanoscale Horiz* **2020**, *5*, 954–959.

[31] Yan, J. H.; Yang, X. Z.; Liu, X. Y.; Du, C.; Qin, F.; Yang, M. M.; Zheng, Z. Q.; Li, J. B. van der Waals heterostructures with built-in Mie resonances for polarization-sensitive photodetection. *Adv. Sci.* **2023**, *10*, 2207022.

[32] Zhou, L.; Huang, S. X.; Tatsumi, Y.; Wu, L. J.; Guo, H. H.; Bie, Y. Q.; Ueno, K.; Yang, T.; Zhu, Y. M.; Kong, J. et al. Sensitive phonon-based probe for structure identification of 1T′ $MoTe_2$. *J. Am. Chem. Soc.* **2017**, *139*, 8396–8399.

[33] Sorifi, S.; Kaushik, S.; Singh, R. A GaSe/Si-based vertical 2D/3D heterojunction for high-performance self-driven photodetectors. *Nanoscale Adv.* **2022**, *4*, 479–490.

[34] Xu, G. L.; Liu, D. M.; Li, S. Y.; Wu, Y.; Zhang, Z. L.; Wang, S. B.; Huang, Z. K.; Zhang, Y. Z. Binary-ternary transition metal chalcogenides interlayer coupling in van der Waals type-II heterostructure for visible-infrared photodetector with efficient suppression dark currents. *Nano Res.* **2022**, *15*, 2689–2696.

[35] Kong, L. X.; Li, G. L.; Su, Q.; Tan, X. H.; Zhang, X. N.; Liu, Z. Y.; Liao, G. L.; Sun, B.; Shi, T. L. Polarization-sensitive, self-powered, and broadband semimetal $MoTe_2/MoS_2$ van der Waals heterojunction for photodetection and imaging. *ACS Appl. Mater. Interfaces* **2023**, *15*, 43135–43144.

[36] Yang, Y. S.; Liu, S. C.; Yang, W.; Li, Z. B.; Wang, Y.; Wang, X.; Zhang, S. S.; Zhang, Y.; Long, M. S.; Zhang, G. M. et al. Air-stable in-plane anisotropic $GeSe_2$ for highly polarization-sensitive photodetection in short wave region. *J. Am. Chem. Soc.* **2018**, *140*, 4150–4156.

[37] Wang, Y.; Wu, P. S.; Wang, Z.; Luo, M.; Zhong, F.; Ge, X.; Zhang, K.; Peng, M.; Ye, Y.; Li, Q. et al. Air-stable low-symmetry narrow-bandgap 2D sulfide niobium for polarization photodetection. *Adv. Mater.* **2020**, *32*, 2005037.

[38] Ahn, J.; Kyhm, J. H.; Kang, H. K.; Kwon, N.; Kim, H. K.; Park, S.; Hwang, D. K. 2D $MoTe_2/ReS_2$ van der Waals heterostructure for high-performance and linear polarization-sensitive photodetector. *ACS Photonics* **2021**, *8*, 2650–2658.

[39] Ding, J. F.; Liu, X. Y.; Gao, Y. Y.; Dong, C.; Yue, G. T.; Tan, F. R. Charge carrier management via semiconducting matrix for efficient self-powered quantum dot infrared photodetectors. *J. Semicond.* **2025**, *46*, 032401.

[40] Liang, G. X.; Li, C. H.; Zhao, J.; Fu, Y.; Yu, Z. X.; Zheng, Z. H.; Su, Z. H.; Fan, P.; Zhang, X. H.; Luo, J. T. et al. Self-powered broadband kesterite photodetector with ultrahigh specific detectivity for weak light applications. *SusMat* **2023**, *3*, 682–696.

[41] Zhong, J. H.; Yu, J.; Cao, L. K.; Zeng, C.; Ding, J. N.; Cong, C. X.; Liu, Z. W.; Liu, Y. P. High-performance polarization-sensitive photodetector based on a few-layered $PdSe_2$ nanosheet. *Nano Res.* **2020**, *13*, 1780–1786.

[42] Wang, F.; Zhang, T.; Xie, R. Z.; Wang, Z.; Hu, W. D. How to characterize figures of merit of two-dimensional photodetectors. *Nat. Commun.* **2023**, *14*, 2224.

[43] Qiu, Q. X.; Huang, Z. M. Photodetectors of 2D materials from ultraviolet to terahertz waves. *Adv. Mater.* **2021**, *33*, 2008126.

[44] Chen, S.; Fu, Y.; Ishaq, M.; Li, C. H.; Ren, D. L.; Su, Z. H.; Qiao, X.; Fan, P.; Liang, G. X.; Tang, J. Carrier recombination suppression and transport enhancement enable high-performance self-powered broadband Sb_2Se_3 photodetectors. *InfoMat* **2023**, *5*, e12400.

[45] Zhou, W.; Chen, J. Z.; Gao, H.; Hu, T.; Ruan, S. C.; Stroppa, A.; Ren, W. Anomalous and polarization-sensitive photoresponse of T_d-WTe_2 from visible to infrared light. *Adv. Mater.* **2019**, *31*, 1804629.

[46] Sun, J.; Ding, L. M. A polarization-sensitive photodetector with patterned $CH_3NH_3PbCl_3$ film. *Small* **2024**, *20*, 2308583.

[47] Chen, Y. F.; Wang, Y.; Wang, Z.; Gu, Y.; Ye, Y.; Chai, X. L.; Ye, J. F.; Chen, Y.; Xie, R. Z.; Zhou, Y. et al. Unipolar barrier photodetectors based on van der Waals heterostructures. *Nat. Electron.* **2021**, *4*, 357–363.